

Corry et al., <http://www.jgp.org/cgi/content/full/jgp.200910376/DC1>

Analysis of FRET data

The efficiency with which the protein is labeled with fluorophores can influence the interpretation of the FRET data. As seen in Fig. S1, however, provided the labeling efficiency is >90%, the results are indistinguishable from 100% labeling.

A more detailed analysis of the pixel by pixel FRET data are shown in Fig. S2 A, in which the relative frequency of each transfer efficiency value is shown for two example mutants before and after the addition of LPC. A small but significant change in the FRET efficiency can be seen for V120C before and after the addition of LPC, and a much greater change is visible for M42C. In Fig. S2 B, results are shown for a situation in which one liposome containing M42C mutant is contained within another after the addition of LPC. The distribution of efficiencies for the outer liposome (red), which is effected by the presence of LPC and in which the channels will be in their open state, are clearly distinguishable from those for the inner liposome (black) in which the channels are likely to remain closed. This result forms an internal control, and similar results were obtained in four other mutants in which unilamellar liposomes could be found contained within one another (K5C, S2C, A27C, and V33C). This reinforces the claim that a

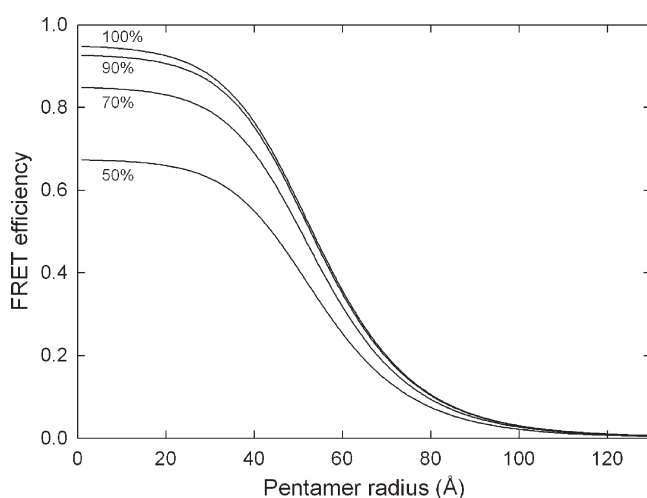


Figure S1. Relationship between FRET efficiency and MscL pentamer radius, as calculated using the program exiFRET (Corry et al., 2005). Plot shows the relationship with equal probability of donor and acceptor labeling at each site. The influence of labeling efficiency is also shown, with data included assuming 100, 90, 70, and 50% efficiency. Note that distance changes are less susceptible to the labeling efficiency than are absolute measurements, and that results with >90% efficiency will be indistinguishable from those with 100%.

substantial change in FRET efficiency occurs in these situations due to the insertion of LPC into the outer liposome.

Additional confocal fluorescence images are shown in Fig. S3.

Measurement of fluorophore orientations

To ascertain that changes in FRET efficiency before and after the addition of LPC represent underlying structural changes of the protein rather than changes in the orientation of the fluorophores, we measured the B factor relating to the average orientation and mobility of the fluorophores, and from this the most likely value of the orientation factor (κ^2) for energy transfer between them, following the procedure developed previously (Corry et al., 2006). There appears to be no significant difference in the value of the orientation factor before and after the addition of LPC (Table S1), indicating that the changes in FRET efficiency reflect underlying increases in the distances between fluorophores at

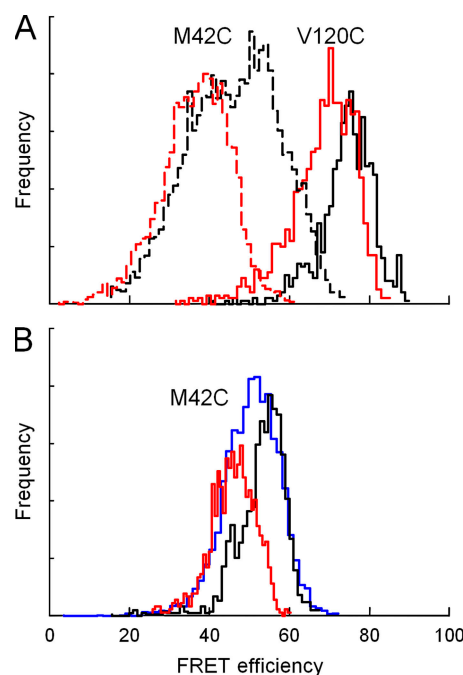


Figure S2. FRET efficiency from pixel by pixel analysis. (A) Histogram showing the relative frequency of each transfer efficiency value, which is indicated for an image of V120C (solid lines) and M42C (dashed lines) mutants before (black) and after (red) the addition of LPC. (B) Efficiency histograms obtained for the inner (black), outer (red), and total (blue) liposomes of the M42C mutant shown in row 3 of Fig. 1 in the main text, obtained after the addition of LPC.

tached to each of the subunits. Furthermore, the use of a value for the orientation factor (κ^2) close to 2/3 appears to be justified.

Additional patch recordings

Patch clamp recordings from fluorophore-labeled channels obtained under pipette suction are shown in Fig. S4. Traces are not shown for M42C, which has been published previously (Corry et al., 2005). Recordings from unlabeled channels obtained in the absence or presence of 25 mM DTT (final concentration) are shown in Fig. S5. The channel reconstitution into liposomes was done using a sucrose method recently developed in our laboratory (Battle et al., 2009). The unlabeled channels behaved differently compared with the labeled channels. In experiments performed with A27C mutant, only channels gating at subconducting levels were observed in 17% of patches ($n = 16$) in the absence of 25 mM DTT (Fig. S5 A, top left panel). In contrast, the activity of fully open channels was recorded in 17% of patches ($n = 58$) examined in the presence of 25 mM DTT (Fig. S5 A, top right panel), comparable to results obtained with the labeled channels shown in Fig.

S4. The application of LPC activated A27C channels in the absence and presence of 25 mM DTT added to the bath with partially as well as fully activated channels in $\sim 25\%$ of patches examined ($n = 10$ and $n = 12$, respectively; Fig. S5 A, bottom panels). In experiments performed with V120C mutant channels, fully and partially activated channels were recorded from $\sim 20\%$ patches in the absence of DTT ($n = 10$; Fig. S5 B, top left panel), whereas fully open channels were recorded in 53% of patches ($n = 19$) in the presence of DTT (Fig. S5 B, top right panel). The application of LPC activated V120C channels in the absence as well as in the presence of 25 mM DTT in $\sim 20\%$ of the patches ($n = 10$ in both cases), with channels exhibiting longer openings in the presence of 25 mM DTT (Fig. S5 B, bottom right panel).

Additional simulation data

The simulation system used for constrained molecular dynamics is shown in Fig. S6. In Fig. S7 A, we indicate the evolution of the RMSD of the protein structure from the initial closed structure during the simulations. The gradual introduction of restraints yields a gradual change in the protein structure, whereas a larger sur-

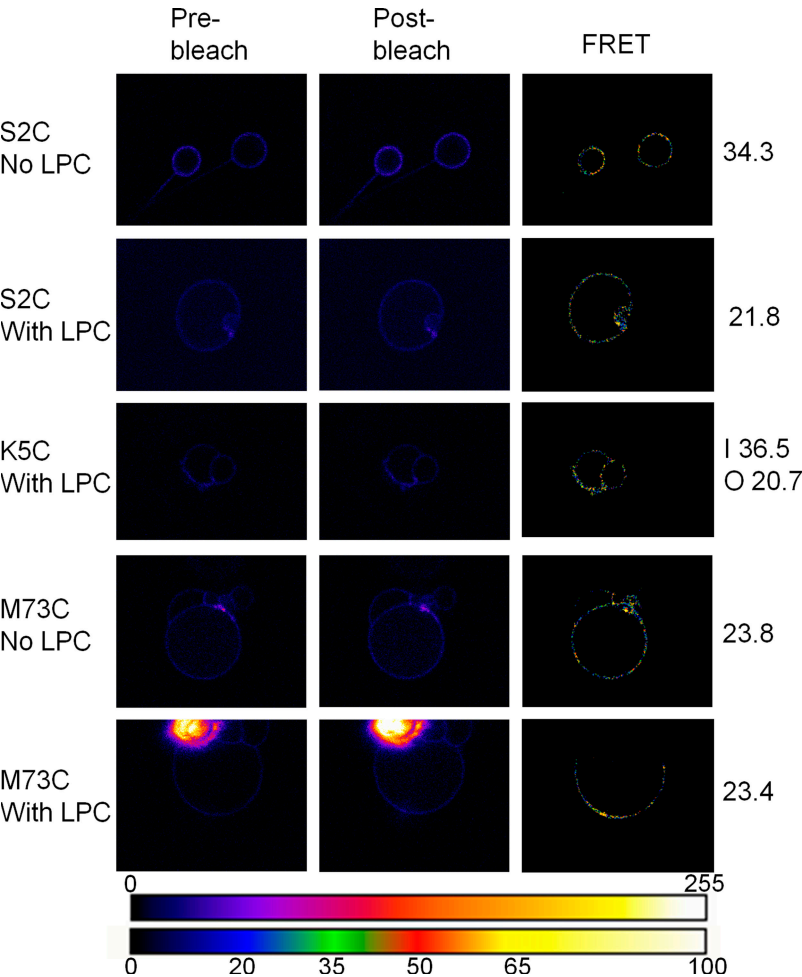


Figure S3. Additional confocal fluorescence images of AF488- and AF568-labeled MscL protein reconstituted into liposomes. Images of the donor (AF488) are shown before (left column) and after (middle column) acceptor photobleaching. Images are colored by intensity according to the top scale bar. An image created from pixel by pixel analysis of the FRET efficiency is shown in the right column, colored according to the bottom scale bar. The mutant name and conditions are noted on the left, and the average FRET efficiency for the image is noted on the right. I, inner liposome; O, outer liposome.

face tension on the membrane leads to a larger conformational change from the closed state. Notably, the RMSD approaches a stable value toward the end of the simulations.

The thickness of the membrane plays an important role in determining the final structure of the protein in our simulations. In Fig. S7 B we plot the bilayer thickness, defined as the average separation of the phosphate groups in each leaflet. A POPC membrane is expected to have a thickness of around 36 Å (Nagle and Tristram-Nagle, 2000). In a simulation of MscL in the absence of experimental restraints, this thickness is found to be slightly less, as indicated by the black line. Remarkably, when the experimental restraints are applied in the absence of surface tension, the bilayer thickness increases and the position of the head groups becomes more disordered due to the presence of local curvature, as can be seen in Fig. 5 of the main text. As suspected, however, the inclusion of surface tension thins the membrane. The thickness of the membrane under 5 mN/m of surface tension is between 1 and 4 Å thinner than in the absence of surface tension, whereas under 60 mN/m, it is 4–7 Å thinner.

To illustrate the nature of the structural changes taking place during the simulation, we plot the tilt of the TM1 and TM2 helices, as well as the average distance between residues in adjacent subunits in the region of the channel gate (residues 21–25) in Fig. S7 (C–E). The tilt on the TM helices is much greater when surface tension is applied to the membrane, but it can be seen that the changes occur smoothly, approaching a stable configuration toward the end of the simulation. The behavior of the C terminus provides an exception to the smooth changes seen elsewhere in the protein, as illustrated in Fig. 6 F.

A structurally ill-defined periplasmic loop connects the TM1 and TM2 helices of MscL, which has been proposed to function as a spring resisting the channel opening (Ajouz et al., 2000; Park et al., 2004), a view supported by a recent molecular dynamics study (Meyer et al., 2006). The periplasmic loops are relatively mobile in our simulations, with major differences in their position on each of the subunits and in each of the simulations. Thus, it is difficult to infer much about this region.

The C-terminal domain, which forms an α -helical bundle at the cytoplasmic end of the MscL channel (Chang et al., 1998), is likely to be the least important structural domain for channel gating, as deletions of a large portion of the domain do not significantly affect mechanosensitivity (Blount et al., 1996; Sukharev et al., 2001; Betanzos et al., 2002). This domain may function as a size-exclusion filter preventing loss of cellular metabolites essential for survival of a bacterial cell (Anishkin et al., 2003), or participate in gating (Yoshimura et al., 2008). Its structural stability, however, is pH dependent (Kocer et al., 2006), suggesting that it may influence the channel gating in a pH-dependent manner. Large structural changes arise in the C-terminal domain in our simulations, with the top of the helical bundle moving apart. Our FRET data for V120C suggest dissociation of the bundle at this position, a result which is consistent with the recent findings of an MscL electron microscopic study showing that MscL opening is accompanied by the dissociation of the C-terminal domain (Yoshimura et al., 2008). Although the function of this domain remains unclear, once apart, large osmolytes can be expected to move more easily between the helices of the dissociated C terminus. In Fig. S7 F, we show the evolution of the distance between the C α atoms in

Table S1
Measurements of fluorophore orientations and mobility

Mutant	B donor pre	B donor post	B acc pre	B acc post	κ^2 pre	κ^2 post
S2C	−0.03 (1)	−0.06 ± 0.02 (2)	−0.16 ± 0.01 (2)	−0.11 ± 0.03 (2)	0.66	0.66
M12C	−0.06 ± 0.01 (5)	−0.04 ± 0.02 (4)	−0.19 ± 0.03 (5)	−0.15 ± 0.02 (4)	0.67	0.66
G14C	−0.07 (1)	−0.11 (1)	−0.12 (1)	−0.17 (1)	0.67	0.67
A27C	−0.11 (1)	−0.06 ± 0.02 (2)	−0.09 (1)	−0.05 ± 0.04 (2)	0.66	0.66
V33C	−0.12 ± 0.03 (2)	−0.07 ± 0.01 (3)	−0.21 ± 0.01 (2)	−0.16 ± 0.03 (3)	0.69	0.67
M42C	−0.12 ± 0.01 (5)	−0.14 ± 0.03 (2)	−0.19 ± 0.03 (4)	−0.22 ± 0.02 (2)	0.69	0.70
K55C	−0.08 ± 0.05 (3)	−0.07 ± 0.03 (4)	−0.15 ± 0.01 (3)	−0.17 ± 0.01 (3)	0.67	0.67
I86C	−0.09 (1)	−0.06 ± 0.02 (2)	−0.18 (1)	−0.15 ± 0.02 (2)	0.67	0.67
M94C	−0.13 ± 0.01 (6)	−0.12 ± 0.01 (4)	−0.13 ± 0.01 (4)	−0.14 ± 0.01 (4)	0.67	0.67
V120C	−0.11 ± 0.02 (8)	−0.11 ± 0.05 (2)	−0.05 ± 0.02 (9)	−0.18 ± 0.03 (2)	0.66	0.68

The “B factor” related to the average orientation of the fluorophores relative to the membrane and their mobility (Corry et al., 2006) is shown for the donor (AF488) and acceptor (AF568) fluorophores before and after the addition of LPC. The most likely value of the orientation factor for energy transfer is also shown.

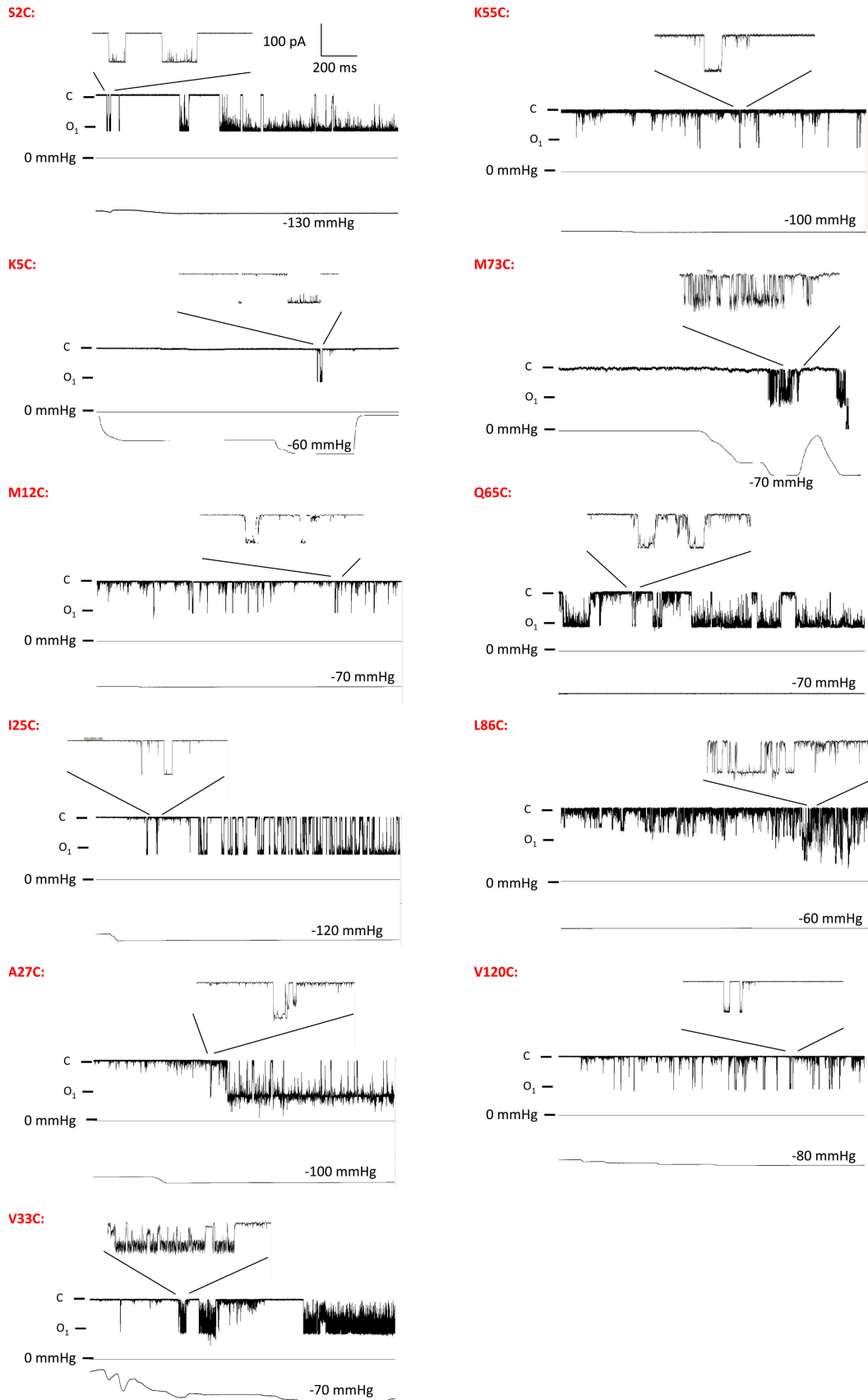


Figure S4. Representative recording traces for fluorophore-labeled channel mutants activated by pipette suction with an applied potential of -30 mV. For each mutant, a longer recording trace and an inset with the enlarged recording trace are shown. Note the different

residue V120 in adjacent subunits in the three simulations. These restraints act to force this section of the bundle apart, but it is notable that the bundle remains intact until quite large experimental restraints are used, suggesting that the helical bundle is relatively stable.

The radius of the channel structures obtained here is compared with the closed-state structures and the open-state model of Meyer (2007) in Fig. S8. We also plot here the current-voltage relationship found using Brownian dynamics simulations incorporating our open-state model.

To assess the stability of our final open-state model, we examine the behavior when either the experimental restraints or both the restraints and membrane tension are removed. To do this, we started from the structure found with 60 mN/m of surface tension and ran a further 5 ns of simulations for each situation. As can be seen in Fig. S9, the pore radius remains relatively constant after the removal of these constraints, and only minor rearrangements of the protein are observed. When both the experimental restraints and membrane tension are both removed, however, the pore begins to shrink, as may be expected if it were returning to the closed state.

In Fig. S10, we show the solvent-accessible surface of the resulting protein structure, indicating that the helices form a channel wall without gaps to the membrane.

A comparison of our open-channel structure and the result of rotating elements of the SaMscL crystal structure along the lines suggested by Liu et al. (2009) to be involved in channel opening is shown in Fig. S11. It can be seen that rotating TM1 and TM2 of the adjacent subunit as a rigid block about an axis perpendicular to the plane of the membrane and passing through G48 results in an open-channel structure with the TM helices placed in almost identical positions to that seen in our open-state model.

REFERENCES

Ajouz, B., C. Berrier, M. Besnard, B. Martinac, and A. Ghazi. 2000. Contributions of the different extramembranous domains of the mechanosensitive ion channel MscL to its response to membrane tension. *J. Biol. Chem.* 275:1015–1022. doi:10.1074/jbc.275.2.1015

Anishkin, A., V. Gendel, N.A. Sharifi, C.S. Chiang, L. Shirinian, H.R. Guy, and S. Sukharev. 2003. On the conformation of the COOH-terminal domain of the large mechanosensitive channel MscL. *J. Gen. Physiol.* 121:227–244. doi:10.1085/jgp.20028768

Battle, A.R., E. Petrov, P. Pal, and B. Martinac. 2009. Rapid and improved reconstitution of bacterial mechanosensitive ion channel proteins MscS and MscL into liposomes using a modified sucrose method. *FEBS Lett.* 583:407–412. doi:10.1016/j.febslet.2008.12.033

Betanzos, M., C.S. Chiang, H.R. Guy, and S. Sukharev. 2002. A large iris-like expansion of a mechanosensitive channel protein induced by membrane tension. *Nat. Struct. Biol.* 9:704–710. doi:10.1038/nsb828

Blount, P., S.I. Sukharev, P.C. Moe, M.J. Schroeder, H.R. Guy, and C. Kung. 1996. Membrane topology and multimeric structure of a mechanosensitive channel protein of *Escherichia coli*. *EMBO J.* 15:4798–4805.

Chang, G., R.H. Spencer, A.T. Lee, M.T. Barclay, and D.C. Rees. 1998. Structure of the MscL homolog from *Mycobacterium tuberculosis*: a gated mechanosensitive ion channel. *Science*. 282:2220–2226. doi:10.1126/science.282.5397.2220

Corry, B. 2006. An energy-efficient gating mechanism in the acetylcholine receptor channel suggested by molecular and Brownian dynamics. *Biophys. J.* 90:799–810. doi:10.1529/biophysj.105.067868

Corry, B., P. Rigby, Z.W. Liu, and B. Martinac. 2005. Conformational changes involved in MscL channel gating measured using FRET spectroscopy. *Biophys. J.* 89:L49–L51. doi:10.1529/biophysj.105.072009

Corry, B., D. Jayatilaka, B. Martinac, and P. Rigby. 2006. Determination of the orientational distribution and orientation factor for transfer between membrane-bound fluorophores using a confocal microscope. *Biophys. J.* 91:1032–1045. doi:10.1529/biophysj.106.080713

Kocer, A., M. Walko, E. Bulten, E. Halza, B.L. Feringa, and W. Meijberg. 2006. Rationally designed chemical modulators convert a bacterial channel protein into a pH-sensory valve. *Angew. Chem. Int. Ed. Engl.* 45:3126–3130.

Liu, Z., C.S. Gandhi, and D.C. Rees. 2009. Structure of a tetrameric MscL in an expanded intermediate state. *Nature*. 461:120–124. doi:10.1038/nature08277

Meyer, G.R. 2007. Electron paramagnetic resonance spectroscopy and computer modelling studies of the structure of prokaryotic mechanosensitive channels. PhD Thesis. University of Queensland, Queensland, Australia. 132 pp.

Meyer, G.R., J. Gullingsrud, K. Schulten, and B. Martinac. 2006. Molecular dynamics study of MscL interactions with a curved lipid bilayer. *Biophys. J.* 91:1630–1637. doi:10.1529/biophysj.106.080721

Nagle, J.F., and S. Tristram-Nagle. 2000. Structure of lipid bilayers. *Biochim. Biophys. Acta.* 1469:159–195.

Park, K.H., C. Berrier, B. Martinac, and A. Ghazi. 2004. Purification and functional reconstitution of N- and C-halves of the MscL channel. *Biophys. J.* 86:2129–2136. doi:10.1016/S0006-3495(04)74272-1

Sukharev, S., M. Betanzos, C.S. Chiang, and H.R. Guy. 2001. The gating mechanism of the large mechanosensitive channel MscL. *Nature*. 409:720–724. doi:10.1038/35055559

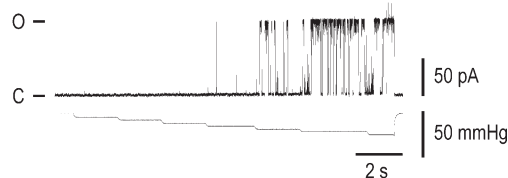
Yoshimura, K., J. Usukura, and M. Sokabe. 2008. Gating-associated conformational changes in the mechanosensitive channel MscL. *Proc. Natl. Acad. Sci. USA.* 105:4033–4038. doi:10.1073/pnas.0709436105

A A27C

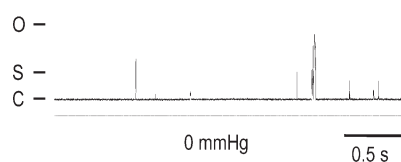
(i) No DTT



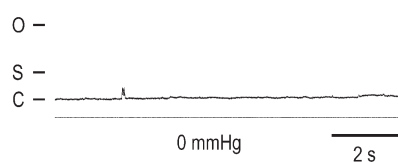
(ii) 25 mM DTT



(iii) No DTT + 10 μ M LPC

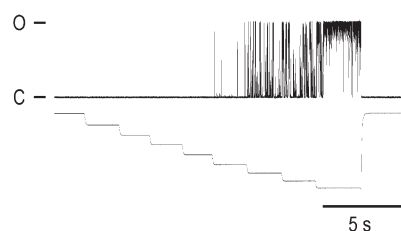


(iv) 25 mM DTT + 10 μ M LPC

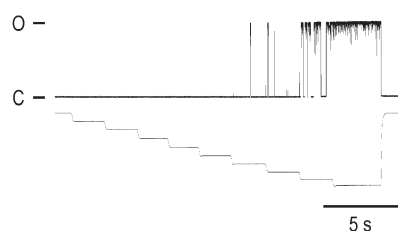


B V120C

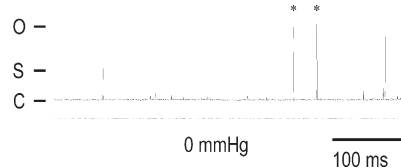
(i) No DTT



(ii) 25 mM DTT



(iii) No DTT + 10 μ M LPC



(iv) 25 mM DTT + 10 μ M LPC

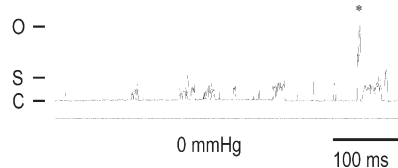


Figure S5. Patch clamp recording from purified MscL mutants A27C (A) and V120C (B), reconstituted into azolectin liposomes upon the application of membrane tension or 10 μ M LPC in the absence or presence of 25 mM DTT. Each recording shows the current (top trace) with or without suction applied (bottom trace). The records from an excised patch in the absence of DTT (i), the application of 25 mM DTT (ii), the application of 10 μ M LPC in the absence of DTT (iii), and in the presence of 25 mM DTT after the addition of 10 μ M LPC (iv). Pipette potential was +30 mV. The asterisk indicates the fully open state. C, S, and O indicate closed, subconducting, and open states, respectively.

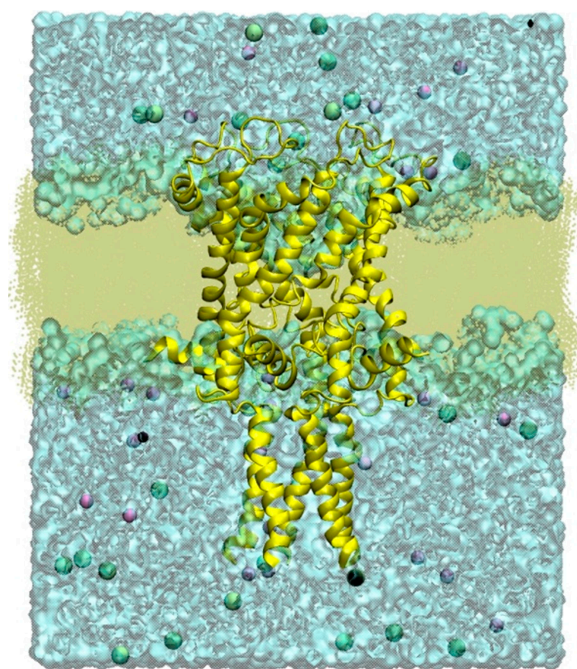


Figure S6. Simulation system. The protein (yellow) is placed in a lipid bilayer (brown) and solvated in a water box containing K⁺ (purple) and Cl⁻ (cyan).

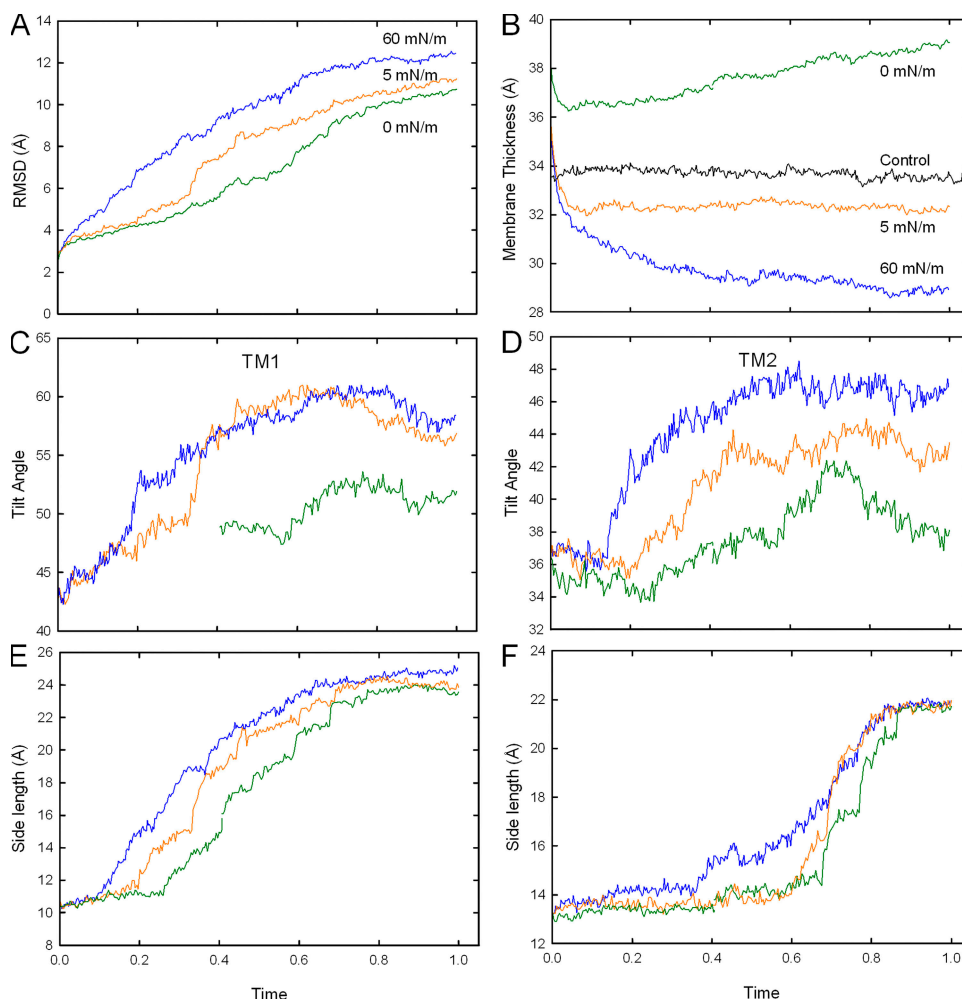


Figure S7. Additional data from molecular dynamics simulations. For each of the simulations we show: (A) the root mean-square deviation of the protein backbone from the initial closed structure; (B) the membrane thickness; the tilt in the TM1 (C) and TM2 (D) helix relative to the membrane; (E) the average distance between the five residues forming the channel gate in adjacent subunits (residues 21–25); and (F) the distance between residue V120 in adjacent subunits. Results are shown with surface tension of 0 (green), 5 (orange), and 60 mN/m (blue). Additional data on the membrane thickness in the absence of experimental restraints are shown by the black line in B. The time axis is represented as the proportion of the total simulation time, which was 18 ns for the 60-mN/m simulation and 13 ns for 0 and 5 mN/m.

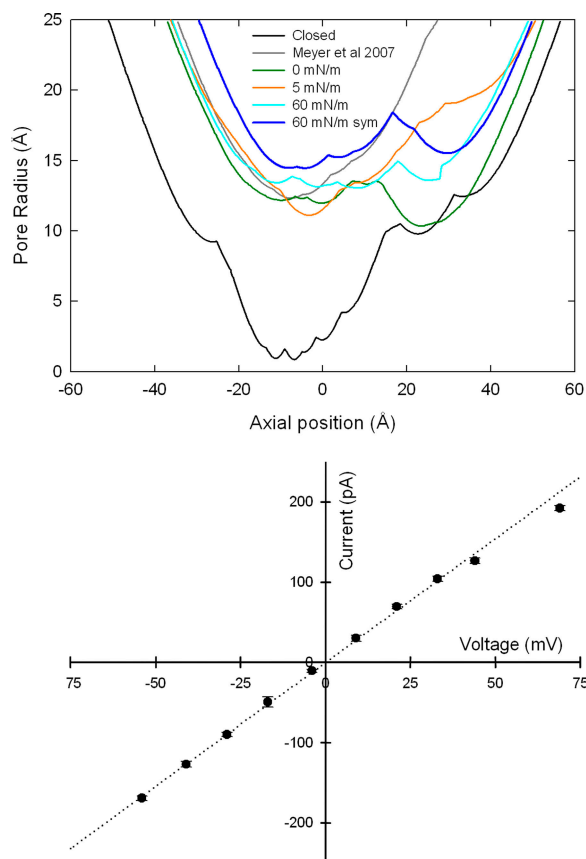


Figure S8. Pore radii and current found for the closed- and open-state models of MscL. (A) Radii are shown for our models found under membrane surface tension of 0 (green), 5 (orange), and 60 mN/m (blue), as well as for the open-state model of Meyer (2007) (gray). Note that the C-terminal domain is not included in calculating the radii in any of the open-state models. (B) Current-voltage relationship calculated using Brownian dynamics simulations for the open-state structure found with no surface tension.

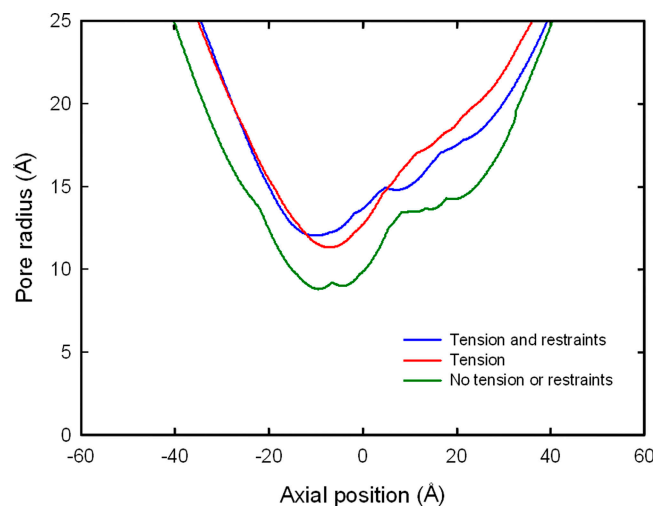


Figure S9. Pore radii found after releasing the experimental restraints (red) or both the restraints and membrane tension (green) starting from the final structure found with 60 mN/m of surface tension (blue).

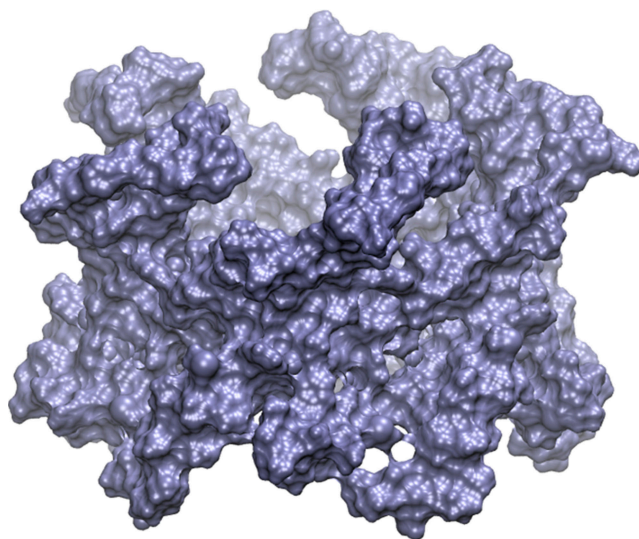


Figure S10. The solvent-accessible surface of the TM regions of the protein is shown to indicate the integrity of the channel wall.

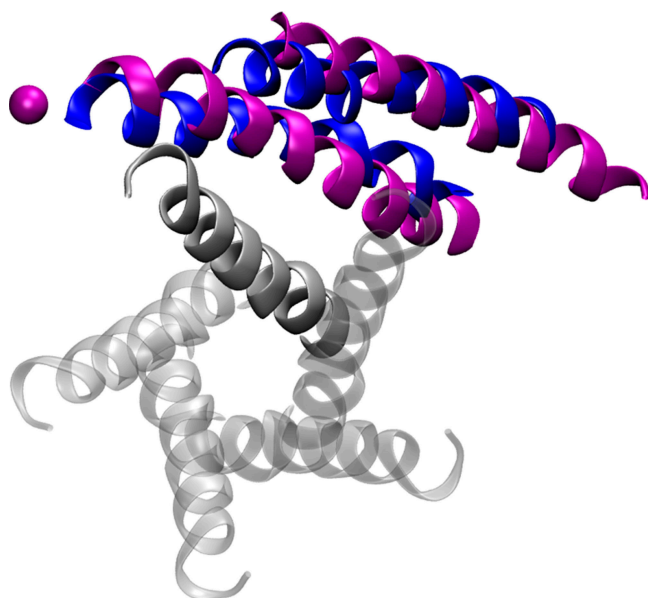
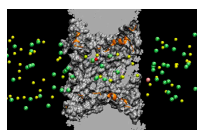


Figure S11. Comparison of our open-channel structure (blue) to that found by “opening” the intermediate SaMScL structure along the lines suggested by Liu et al. (2009) (purple), rotating TM1 and TM2 of the adjacent subunit as a rigid block about an axis perpendicular to the plane of the membrane, and passing through G48 results in an open-channel structure with the TM helices placed in almost identical positions to that seen in our open-state model. The position of TM1 in the closed-state structure is shown in gray for comparison.



Video 1. Brownian dynamics simulation of ion permeation through the proposed open structure of MscL under 100 mV of driving potential with 300 mM KCl. K^+ is shown in yellow and Cl^- in green, apart from one K^+ that is shown in red and one Cl^- shown in pink to more clearly see the motion of these ions through the pore.